

Compressible Turbulence as a Source of Particle Beams and Ion Bernstein Waves in Collisionless Plasmas

Chuanpeng Hou,^{1,*} Huirong Yan,^{2,1,†} and Siqi Zhao¹

¹*Institut für Physik und Astronomie, Universität Potsdam, D-14476 Potsdam, Germany*

²*Deutsches Elektronen Synchrotron (DESY), Platanenallee 6, D-15738 Zeuthen, Germany*

(Dated: January 29, 2026)

We investigate the source of particle beams and ion Bernstein waves in collisionless plasmas using a high-resolution particle-in-cell simulation of compressible turbulence. At magnetohydrodynamic (MHD) scales, compressible turbulence is damped by transit-time damping, naturally generating suprathermal electrons and proton beams. As the energy cascade reaches sub-ion scales, multiple branches of ion Bernstein waves are excited and contribute to the formation of proton suprathermal tails. Under realistic conditions such as those in the solar wind, these processes remain efficient and provide a natural explanation for the super-Alfvénic proton beams observed in situ. We show that compressive fluctuations, though often understudied, are essential for cross-scale energy transfer and dissipation in collisionless plasma turbulence.

I. INTRODUCTION

As coronal plasma expands into the turbulent solar wind, its temperature decreases more slowly than predicted by adiabatic models, giving rise to the long-standing solar wind heating problem [1]. In-situ measurements provide direct evidence that solar wind heating is associated with non-Maxwellian particle velocity distributions [2]. Such proton velocities frequently exhibit a core-beam distribution, with a beam population drifting along the magnetic field direction [3]. Observations further show that the drift speed between the proton core and beam often exceeds the local Alfvén speed and increases with plasma β [4]. Near-Sun measurements by Parker Solar Probe indicate that the beam speed averages around $\sim 2.5v_A$ [5]. In the weakly collisional solar wind, such proton beams carry substantial free energy, can excite ion-scale waves, and are therefore widely regarded as an important energy source for solar wind heating [2, 6, 7]. Numerous mechanisms have been proposed to explain beam formation, including Coulomb collisions, cyclotron resonance, magnetic reconnection, and parametric instabilities of Alfvén waves [8–11]. However, no unified physical picture has been provided on the source of proton beams.

Kinetic waves play another key role in solar wind heating. In addition to whistler, ion cyclotron, and kinetic Alfvén waves [12–14], recent high-resolution measurements from Cluster and MMS spacecraft have revealed the presence of ion Bernstein waves (IBWs) in both the solar wind and the Earth’s magnetosheath [15–17]. IBWs can heat ions through cyclotron resonance and participate in mode conversion with kinetic Alfvén waves, providing additional pathways for energy transfer [18]. Similar to proton beams, the source of IBWs remains debated, with proposed mechanisms including turbulent cascades

to sub-ion scales and local driving by non-thermal ion distributions [15, 16].

A key step toward resolving these issues is to distinguish the role of compressible turbulence [19–23]. While early studies focused primarily on incompressible Alfvénic turbulence [24], recent PSP observations show that compressible fast magnetosonic waves also carry a significant fraction of the turbulent energy in the solar wind [25]. Understanding how this compressible energy is dissipated and transferred across scales therefore becomes essential. Compressible turbulence dominated by fast magnetosonic waves are expected to dissipate efficiently at magnetohydrodynamic (MHD) scales via transit-time damping (TTD), resulting in particle heating [26, 27], while wave steepening may further contribute to the generation of sub-ion fluctuations [28].

In this work, we investigate the evolution of compressible turbulence from magnetohydrodynamic (MHD) to sub-ion scales using 2.5D fully kinetic particle-in-cell simulations. We show that particle beams and IBWs are naturally generated during this evolution, providing a unified framework that links compressible turbulence, kinetic wave generation, and particle heating.

Our high spatial and temporal resolution compressible turbulence simulation is performed using the VPIC code [29]. This decaying compressible turbulence with periodic boundary is initialized by superposing fast waves with wave vectors $(k_0, 2k_0, 3k_0)$ along each dimension, where $k_0 = 2\pi/L_0$ and L_0 is the box size. Integer wave vectors ensure periodic continuity. The domain size is $256d_i \times 256d_i$, resolved by 4096^2 cells ($\Delta x = 0.0625d_i$), where $d_i = v_A/\Omega_p$ is the proton inertial length, v_A is the Alfvén speed, and Ω_p is the proton gyrofrequency. Both protons and electrons are treated kinetically with a reduced mass ratio $m_p/m_e = 10$, using 500 particles per species per cell. Particles are initialized with plasma $\beta = 0.5$ and equal initial temperatures ($T_{p,0} = T_{e,0}$). The time step $\Delta t = 0.00625\Omega_p^{-1} = 0.0625\Omega_e^{-1}$ ensures adequate resolution of electron dynamics. The initial electromagnetic fields and particle moments follow fast-wave po-

* Humboldt Research Fellow.

† huirong.yan@desy.de

larization relations, with random phases and equal amplitudes, yielding $\delta v_{\text{rms}}/v_A \simeq 0.23$, where $\delta v_{\text{rms}} = \sqrt{\langle |\delta v|^2 \rangle}$ denotes the root-mean-square of velocity fluctuation.

II. RESULTS AND DISCUSSION

A. Angle-dependent turbulence cascade and damping

Fig. 1a shows that the compressible turbulence develops a pronounced angle-dependent energy distribution in wavenumber space ($k_{\perp} - k_{\parallel}$). This anisotropy arises from two effects. First, for quasi-parallel propagation, density and magnetic-field perturbations are suppressed and fast waves behave similarly to incompressible Alfvén waves, leading to a reduced cascade rate and weaker fluctuation energy along the k_{\parallel} direction [27, 30]. Second, a depletion of fluctuation energy is observed at the propagation angle $\theta_{kB} \approx 40^\circ - 65^\circ$ (Fig. 1(a1)), resulting from TTD via resonant interactions with electrons and protons [21, 27].

The damping rate for TTD at $\beta < 1$ can be written as [26]

$$\Gamma = \frac{\sqrt{\pi\beta} \sin^2 \theta_{kB}}{4 \cos \theta_{kB}} \left[\sqrt{\frac{m_e}{m_p}} \exp\left(-\frac{m_e}{m_p \beta \cos^2 \theta_{kB}}\right) + 5 \exp\left(-\frac{1}{\beta \cos^2 \theta_{kB}}\right) \right] k v_f. \quad (1)$$

where v_f is the fast wave speed.

Eq. 1 depends on both plasma β and the ion-electron mass ratio and could reproduce the angular damping behavior obtained from numerical solver WHAMP [31]. For a realistic mass ratio ($m_p/m_e \approx 1836$) and $\beta = 0.5$, two distinct damping peaks arise, associated with proton resonance at $\theta_{kB} \approx 34^\circ$ and electron resonance near perpendicular propagation $\theta_{kB} \approx 87^\circ$ (Fig. S1). By contrast, for the reduced mass ratio used here, these resonances merge into a single broad angular range at $\theta_{kB} \approx 40^\circ - 65^\circ$ (Fig. 1(a1)).

The effect of TTD is further shown in the 1D power spectra (Fig. 1b). At large scales ($kd_i < 0.15$), the parallel and perpendicular spectra are similar and slightly steeper than -1.5 , consistent with previous studies [27, 32, 33]. At smaller scales ($kd_i > 0.15$), the perpendicular spectrum steepens to nearly -3 , while the parallel spectrum remains close to -1.5 , indicating preferential dissipation of quasi-perpendicular fluctuations. Despite this dissipation, the perpendicular cascade persists to ion scales ($kd_i \approx 1$), where turbulent energy becomes strongly concentrated at perpendicular propagation. Discrete peaks in $PSD(k_{\perp})$ around $kd_i \approx 1$ further indicate that, in addition to the turbulent cascade, fast wave phase steepening may also contribute to the kinetic fluctuations, likely driven by dispersive effects (Movie S1).

The electron parallel temperature ($T_{e,\parallel}$) grows most rapidly, consistent with TTD heating (Fig. 1c), whereas proton parallel heating ($T_{p,\parallel}$) is weaker because fewer

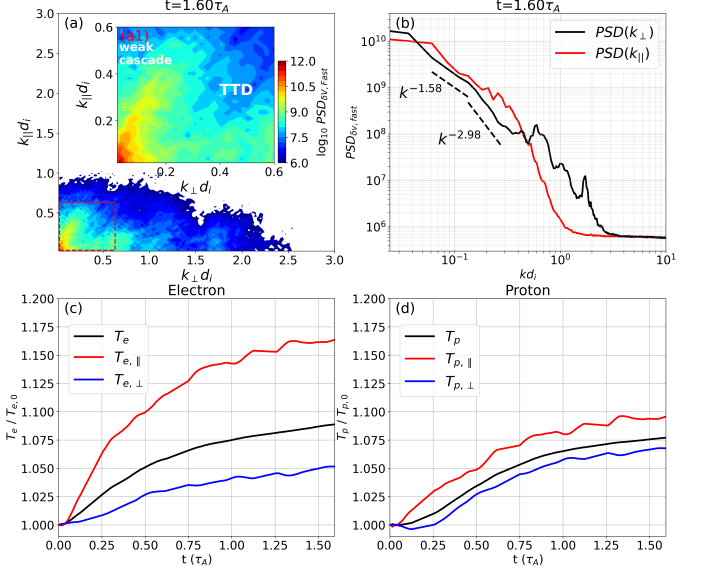


FIG. 1. Energy distribution of compressible turbulence and the evolution of particle temperatures. (a) Energy distribution of compressible turbulence in the $k_{\perp} - k_{\parallel}$ space. (a1) Zoomed-in view corresponding to the red dashed box in panel (a). (b) 1D integrated PSD. (c) Temporal evolution of the electron temperature components, normalized by initial temperature. (d) The same as panel (c) but for protons. An animation for the temporal evolution of electron number density (n_e) is available.

protons satisfy the resonance condition $v_{\parallel} = \omega/k_{\parallel}$ (Fig. 1d) [27]. Additionally, the proton perpendicular temperature ($T_{p,\perp}$) shows a slightly stronger increase than the electron perpendicular temperature ($T_{e,\perp}$), implying an additional proton heating channel, which is attributed to resonant interactions with ion Bernstein waves (Sec. II C).

B. Excitation of ion Bernstein waves

To identify sub-ion-scale waves, we obtain the fluctuation energy distribution in $\omega - k$ space using a three-dimensional Fourier transform and compare the spectra with kinetic dispersion relations computed using PKUES [34]. For nearly perpendicular propagation fluctuations ($k_{\parallel} \approx 0$), most of the fluctuation energy follows the fast wave dispersion relations, indicating the wave-like nature of compressible turbulence [35]. Several discrete branches are observed and are well matched by IBW dispersion relations (Figs. 2(a)–(c)). In contrast, for nearly parallel propagation ($k_{\perp} \approx 0$), the spectra follow the whistler-wave branch and show no discrete features (Figs. 2(d)–(f)), confirming that IBWs in Figs. 2(a)–(c) are not numerical artifacts. Additionally, the correspondence with the lower-hybrid branch is not clear.

The electromagnetic properties further confirm the IBW identification. The perpendicular propagating fluc-

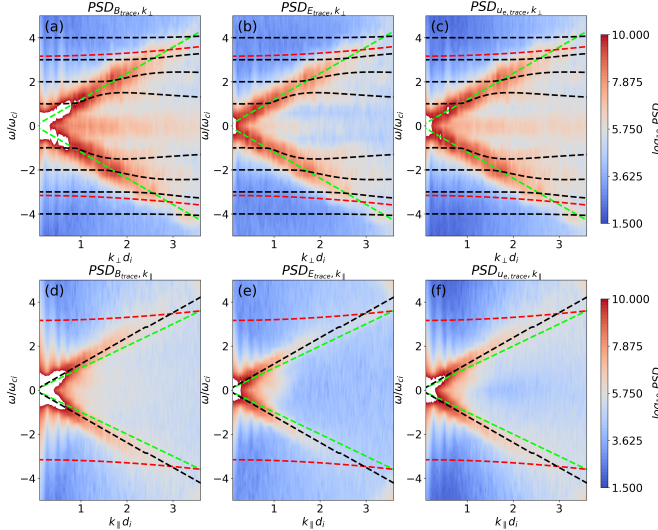


FIG. 2. Dispersion relations at sub-ion scales during the interval $t = 1.51\tau_A$ – $1.60\tau_A$. (a)–(c) PSD Traces of the magnetic-field, electric-field, and electron-velocity fluctuation for perpendicular propagating fluctuations ($k_{\parallel} \approx 0$). The black dashed line shows the theoretical dispersion relation of the ion Bernstein wave, the red line corresponds to the lower-hybrid wave, and the green line denotes the fast wave dispersion $\omega = kv_f$. (d)–(f) PSD Traces of the magnetic-field, electric-field, and electron-velocity fluctuation for parallel propagating fluctuations ($k_{\perp} \approx 0$). In panels (d)–(f), the black dashed line represents the theoretical dispersion relation of whistler waves.

tuations in Figs. 2a–c exhibit nearly linear polarization (Fig. S2(a)), dominant perpendicular electric fields (Fig. S2(b)), quasi-electrostatic character (Fig. S2(c)), and strong compressibility (Fig. S2(d)), all consistent with IBWs' properties. Enhanced fluctuation power near the crossings of fast wave and IBW dispersion branches suggests possible mode conversion, in which fast wave energy is transferred to ion Bernstein waves as the cascade reaches sub-ion scales [36].

At early times ($t = 0.25$ – $0.35\tau_A$), fast waves undergo rapid nonlinear steepening owing to their compressive nature, occurring on timescales of about 1.5 nonlinear times ($\sim 1.5\tau_{nl}$, with $\tau_{nl} = 0.23\tau_A$; see Movie S1). This steepening excites small-scale fast waves through dispersive effects [37] and is accompanied by the appearance of IBWs in the dispersion relations (Fig. S3), demonstrating that IBWs can arise from intrinsic coupling with fast waves at sub-ion scales.

For realistic mass ratios and $\beta = 0.5$, transit-time damping strongly suppresses the cascade of quasi-perpendicular fast waves to sub-ion scales [38, 39], making fast wave steepening the dominant pathway for IBW generation. This mechanism is robust, as it is observed in both 2D PIC and 3D hybrid simulations [27]. However, under appropriate conditions, the turbulent cascade can reach sub-ion scales before being fully dissipated. Equating the damping rate (Eq. 1) with the cascade rate,

$\tau_{\text{cas}}^{-1} \approx (k/L_0)^{1/2} \delta v^2/v_f$ [26, 40], defines a β -dependent truncation scale of the cascade. At low β , the cascade of quasi-perpendicular fast waves can be stronger than the damping, allowing energy to access sub-ion scales. Consequently, suitably injected compressive modes can efficiently cascade to sub-ion scales and excite ion Bernstein waves.

C. Formation of particle beams

The electron VDF in v_{\parallel} – v_{\perp} space (Fig. 3(a)) exhibits a clear beam-like component with parallel velocities exceeding the fast wave speed v_f . The temporal evolution of the parallel VDF (Fig. 3(a1)) shows that the enhancement occurs primarily at $v_{\parallel} \gtrsim v_f$, consistent with transit-time damping (TTD) resonance with fast waves, $v_{e,\parallel} = \omega/k_{\parallel} = v_f/\cos\theta_{kB} \geq v_f$. The strongest enhancement appears near $v_{e,\parallel} = v_f/\cos 45^\circ$. By contrast, the perpendicular electron VDF remains nearly unchanged (Fig. 3(a2)), indicating negligible perpendicular electron heating.

Protons exhibit similar but weaker parallel features. The proton VDF (Fig. 3(b)) shows a beam-like enhancement near v_f . The parallel proton VDF is enhanced at $v_{\parallel} \gtrsim v_f$ (Fig. 3(b1)), again consistent with TTD resonance. Because the proton thermal speed is lower than v_f , fewer protons satisfy the resonance condition, resulting in a weaker proton beam than for electrons. In higher- β plasmas, a larger fraction of protons is expected to resonate with fast waves, leading to increased proton beam density and drift speed.

Unlike electrons, protons exhibit clear perpendicular energization (Fig. 3(b)), with velocity distributions displaying kappa-like suprathermal tails with $\kappa = 4.2$ (Fig. 3(b2)). Notably, enhanced perpendicular velocities are observed even for protons with $v_{p,\parallel} \approx 0$, indicating that this heating is unlikely to result from cyclotron resonance with right-hand polarized whistler waves, which requires $v_{p,\parallel} > v_f$. Instead, the observed behavior is more naturally explained by resonant interactions with ion Bernstein waves [41].

For a realistic mass ratio ($m_p/m_e \approx 1836$), the TTD rate (Eq. 1) implies that protons resonate with fast waves at $\theta_{kB} \sim 30^\circ$ – 50° , with the resonant velocity set by β . For $\beta = 0.5$, the strongest proton-dominated TTD occurs at $\theta_{kB} \approx 34^\circ$, corresponding to a resonant speed $v_{\text{res}} \approx 1.3v_A$ and naturally producing a proton component drifting at the same speed. As β increases, a larger fraction of protons satisfies the resonance condition, and the damping peak shifts toward more oblique propagation. For $\beta = 2$, the resonant velocity increases to $v_{\text{res}} \approx 2.4v_A$, well into the super-Alfvénic regime, consistent with near-Sun PSP observations [5].

Solar wind observations show a positive correlation between proton temperature anisotropy (T_{\parallel}/T_{\perp}) and β , as well as enhanced parallel temperatures in the more compressive slow wind [3, 42]. While multiple processes may

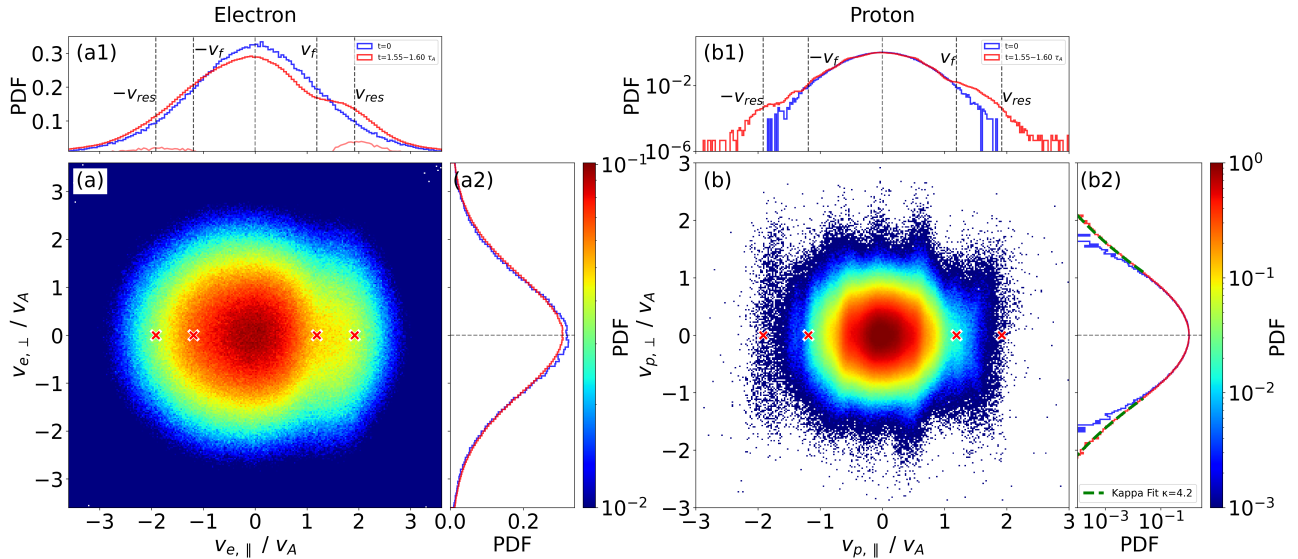


FIG. 3. Particle velocity distributions corresponding to the spatial region ($x = 0-2d_i, y = 0-2d_i$). (a) Electron 2D velocity distribution in the $v_{\parallel}-v_{\perp}$ space. Red crosses mark fast magnetosonic speed v_f and resonant speed v_{res} . (a1) Electron parallel velocity distribution, with dashed lines indicating v_f and v_{res} . (a2) Electron perpendicular velocity distribution. The blue histogram shows the initial distribution at $t = 0$, and the red histogram corresponds to $t = 1.55\tau_A-1.6\tau_A$. The light red lines indicate the difference between the two histograms. (b) Proton 2D velocity distribution in the $v_{\parallel}-v_{\perp}$ space. Red crosses mark v_f and v_{res} . (b1) Proton parallel velocity distribution, with dashed lines indicating v_f and v_{res} . (b2) Proton perpendicular velocity distribution. The blue histogram shows the initial distribution at $t = 0$, and the red histogram corresponds to $t = 1.55\tau_A-1.6\tau_A$. The green dashed lines represent a kappa distribution fit with $\kappa = 4.2$.

contribute to such observations, these correlations are consistent with expectations from TTD. Together, our results show that under realistic solar wind conditions, fast wave dissipation via TTD can efficiently accelerate protons to super-Alfvénic speeds, providing a natural source of particle beams and enhancing parallel heating in the solar wind.

III. CONCLUSION

Our results demonstrate that compressible turbulence dissipates energy not only at sub-ion scales but also at MHD scales. This previously underappreciated MHD-scale dissipation is responsible for generating particle beams. The main results are summarized as follows.

- At MHD scales, TTD of compressible turbulence can drive the formation of particle beams. The proton resonant speed increases with plasma β , allowing the resulting beam drift to become strongly super-Alfvénic under typical solar-wind conditions, consistent with near-Sun PSP observations.
- At sub-ion scales, IBWs are generated, as confirmed by their dispersion relations, quasi-electrostatic nature, and strong compressibility. The proton beam fraction is too small to drive

IBWs via kinetic instabilities. Instead, IBWs emerge from intrinsic coupling with fast waves, facilitated by turbulent cascade and phase steepening. IBWs offer an efficient channel for perpendicular energization of suprathermal protons.

- Under low- β conditions, both the turbulent cascade and phase steepening of quasi-perpendicular fast waves can supply energy to sub-ion scales and act as sources of IBWs. At higher β ($\beta > 1$), strong TTD suppresses the turbulent cascade [38, 39], while enhanced TTD-generated proton beams may provide an additional pathway for IBW excitation through kinetic instabilities.

ACKNOWLEDGMENTS

We acknowledge the computing resources from the high-performance computers at the NHR center NHR@ZIB, with the project No. bbp00080. The VPIC simulation code is available at <https://github.com/lanl/vpic>. We would like to acknowledge the use of ChatGPT for improving the English grammar and sentence structure. C.H. is supported by the Alexander von Humboldt Foundation.

[1] C.-Y. Tu and E. Marsch, *Solar Physics* **171**, 363 (1997).

[2] J. He, L. Wang, C. Tu, E. Marsch, and Q. Zong, *The Astrophysical Journal Letters* **800**, L31 (2015).

[3] J. Huang, J. C. Kasper, D. Vech, K. G. Klein, M. Stevens, M. M. Martinović, B. L. Altermann, T. Ďurovčová, K. Paulson, B. A. Maruca, *et al.*, *The Astrophysical Journal Supplement Series* **246**, 70 (2020).

[4] R. De Marco, R. Bruno, V. K. Jagarlamudi, R. d'Amicis, M. Marcucci, V. Fortunato, D. Perrone, D. Telloni, C. Owen, P. Louarn, *et al.*, *Astronomy & Astrophysics* **669**, A108 (2023).

[5] J. Verniero, B. Chandran, D. Larson, K. Paulson, B. Altermann, S. Badman, S. Bale, J. Bonnell, T. Bowen, T. D. de Wit, *et al.*, *The Astrophysical Journal* **924**, 112 (2022).

[6] L. K. Jian, C. T. Russell, J. G. Luhmann, R. J. Strange-way, J. S. Leisner, and A. B. Galvin, *The Astrophysical Journal* **701**, L105 (2009).

[7] T. A. Bowen, B. D. Chandran, J. Squire, S. D. Bale, D. Duan, K. G. Klein, D. Larson, A. Mallet, M. D. McManus, R. Meyrand, *et al.*, *Physical Review Letters* **129**, 165101 (2022).

[8] S. Livi and E. Marsch, *Journal of Geophysical Research: Space Physics* **92**, 7255 (1987).

[9] C.-Y. Tu, L.-H. Wang, and E. Marsch, *Journal of Geophysical Research: Space Physics* **107**, SSH (2002).

[10] J. A. Araneda, E. Marsch, and A. F.-Viñas, *Physical review letters* **100**, 125003 (2008).

[11] B. Lavraud, R. Kieokaew, N. Fargette, P. Louarn, A. Fedorov, N. Andre, G. Fruit, V. Génot, V. Réville, A. P. Rouillard, *et al.*, *Astronomy & Astrophysics* **656**, A37 (2021).

[12] Y. Tong, I. Y. Vasko, A. V. Artemyev, S. D. Bale, and F. S. Mozer, *The Astrophysical Journal* **878**, 41 (2019).

[13] L. Jian, H. Wei, C. Russell, J. Luhmann, B. Klecker, N. Omidi, P. Isenberg, M. Goldstein, A. Figueroa-Viñas, and X. Blanco-Cano, *The Astrophysical Journal* **786**, 123 (2014).

[14] S. Huang, J. Zhang, F. Sahraoui, J. He, Z. Yuan, N. Andrés, L. Hadid, X. Deng, K. Jiang, L. Yu, *et al.*, *The Astrophysical journal letters* **897**, L3 (2020).

[15] C. J. Joyce, C. W. Smith, P. A. Isenberg, S. P. Gary, N. Murphy, P. C. Gray, and L. F. Burlaga, *The Astrophysical Journal* **745**, 112 (2012).

[16] O. W. Roberts, D. Verscharen, Y. Narita, R. Nakamura, Z. Vörös, and F. Plaschke, *Physical Review Research* **2**, 043253 (2020).

[17] L. Turc, O. W. Roberts, D. Verscharen, A. P. Dimmock, P. Kajdič, M. Palmroth, Y. Pfau-Kempf, A. Johlander, M. Dubart, E. K. Kilpua, *et al.*, *Nature Physics* **19**, 78 (2023).

[18] J. J. Podesta, *Journal of Geophysical Research: Space Physics* **117** (2012).

[19] K. Makwana and H. Yan, *Physical Review X* **10**, 031021 (2020).

[20] H. Zhang, A. Chepurnov, H. Yan, K. Makwana, R. Santos-Lima, and S. Appleby, *Nature Astronomy* **4**, 1001 (2020).

[21] S. Zhao, H. Yan, T. Z. Liu, K. H. Yuen, and M. Shi, *The Astrophysical Journal* **962**, 89 (2024).

[22] P. Pavaskar, K. H. Yuen, H. Yan, and S. Malik, *The Astrophysical Journal* **971**, 58 (2024).

[23] J. Zhang and Y. Hu, *arXiv preprint arXiv:2511.04119* (2025).

[24] L. Adhikari, G. P. Zank, L.-L. Zhao, J. C. Kasper, K. E. Korreck, M. Stevens, A. W. Case, P. Whittlesey, D. Larson, R. Livi, *et al.*, *The Astrophysical Journal Supplement Series* **246**, 38 (2020).

[25] S. Q. Zhao, H. Yan, T. Z. Liu, M. Liu, and M. Shi, *The Astrophysical Journal* **923**, 253 (2021).

[26] H. Yan and A. Lazarian, *The Astrophysical Journal* **614**, 757 (2004).

[27] C. Hou, H. Yan, S. Zhao, and P. Pavaskar, *The Astrophysical Journal Letters* **992**, L28 (2025).

[28] T. K. Suzuki, A. Lazarian, and A. Beresnyak, *The Astrophysical Journal* **662**, 1033 (2007).

[29] K. J. Bowers, B. J. Albright, L. Yin, W. Daughton, V. Roytershteyn, B. Bergen, and T. J. Kwan, in *Journal of Physics: Conference Series*, Vol. 180 (IOP Publishing, 2009) p. 012055.

[30] S. Galtier, *Journal of Plasma Physics* **89**, 905890205 (2023).

[31] S. Zhao, H. Yan, T. Z. Liu, and C. Hou, *The Astrophysical Journal* **996**, 46 (2026).

[32] J. Cho and A. Lazarian, *Physical Review Letters* **88**, 245001 (2002).

[33] S. Zhao, H. Yan, T. Z. Liu, M. Liu, and H. Wang, *The Astrophysical Journal* **937**, 102 (2022).

[34] Q. Luo, X. Zhu, J. He, J. Cui, H. Lai, D. Verscharen, and D. Duan, *The Astrophysical Journal* **928**, 36 (2022).

[35] K. H. Yuen, H. Li, and H. Yan, *The Astrophysical Journal* **986**, 221 (2025).

[36] H. Comišel, Y. Narita, and U. Motschmann, *Earth, Planets and Space* **67**, 32 (2015).

[37] A. Balogh and R. A. Treumann, *Physics of collisionless shocks: space plasma shock waves* (Springer Science & Business Media, 2013).

[38] V. Petrosian, H. Yan, and A. Lazarian, *The Astrophysical Journal* **644**, 603 (2006).

[39] H. Yan and A. Lazarian, *The Astrophysical Journal* **673**, 942 (2008).

[40] J. Cho and A. Lazarian, *MNRAS* **345**, 325 (2003).

[41] Y. Narita, R. Nakamura, W. Baumjohann, K.-H. Glassmeier, U. Motschmann, and H. Comišel, in *Annales Geophysicae*, Vol. 34 (Copernicus Publications Göttingen, Germany, 2016) pp. 85–89.

[42] J. Huang, D. E. Larson, T. Ervin, M. Liu, O. Ortiz, M. M. Martinović, Z. Huang, A. Chasapis, X. Chu, B. Altermann, *et al.*, *The Astrophysical Journal Letters* **986**, L28 (2025).